Lattice Boltzmann Simulation of Falling Film Flow under Low Reynolds Number

Tao Lu and Fu Xiao*

Department of Building Services Engineering, The Hong Kong Polytechnic University, Hong Kong

***Author for correspondence:**

Tel: +852 27664194; Fax: +852 27657198

Email: linda.xiao@polyu.edu.hk

Address: Department of Building Services Engineering, The Hong Kong Polytechnic University, Hung Hom, Kowloon, Hong Kong.

ABSTRACT

In this paper, a new two-dimensional simulation model was developed for the falling film flow under low Reynolds number (below 20). The phase-field multiphase lattice Boltzmann model was developed to simulate the flow pattern of the two-phase falling film with high density ratio. The approaches to treating the liquid-gas interface with high density ratio (up to 775), surface tension, gravity, inlet and outlet open boundary conditions as well as solid-liquid interface considering contact angle were developed firstly, and then implemented in the model. The dynamic characteristics of the film flow, including the development of the liquid-gas interface and the film thickness, were simulated under the Reynolds numbers between 1.0 and 20. The results show that the film is fully laminar under low Reynolds numbers. The falling film flow model developed in this study lays the foundation for the study of heat and mass transfer in the falling film based liquid desiccant dehumidifier.

INTRODUCTION

As a special type of multi-phase flow, falling film is widely used in industries like thermal engineering, energy engineering [1, 2] and air conditioning engineering, especially the liquid desiccant air conditioning [3] due to its simple structure, low temperature difference and considerable heat and mass transfer efficiency. Fig. 1 shows the typical falling film, i.e. a thin liquid film falling down the vertical plate. Fig. 2 is the two-dimensional schematic side view of the falling film. The falling film is usually characterized by a thin liquid layer on an inclined or vertical plate and some gas in the remaining space. Complicated heat and mass transfer process including phase change can occur between the liquid layer and the gas, which makes falling film appropriate for heat and mass exchange. When the desiccant solution (such as the $LiCl_2$ solution) is chosen as the working liquid and the moist air takes the role of gas, the falling desiccant solution film becomes a dehumidifier [4]. It is reported that the liquid desiccant air conditioning system based on this kind of dehumidifier can save about 10-30% of energy compared with the low temperature dehumidification using conventional gas compression system [5]. Thus, it is important and valuable to better understand the characteristics of falling film flow to enhance the mass/moisture transfer.

The study on the falling film phenomenon can be traced back to early 1900s, when Nusselt developed a group of empirical formulas to describe the film flow on an inclined plate with the assumption that the film flow is totally laminar. Since then, various theoretical models have been developed [6-9] and numerous experimental studies [10-14] have been conducted to study the film characteristics, such as film interface instability, generation mechanism of wave, heat transfer between the liquid

and the gas as well as phase change phenomenon. With the development of computational fluid dynamics (CFD), numerical methods become popular in falling film research [15]. Miyara [16] numerically and experimentally studied the relationship between the interface wave and the film Reynolds number Re. They found that when Re < 20 (critical value) the film is totally laminar with the interface being smooth, and sine waves appear when the Re is beyond 20. When Re > 100, the film flow becomes turbulent and is no longer stable. The irregular waves on falling films were theoretically analyzed by Joo and Davis in 1992 [17]. They used a long-wave evolution equation of Benney type to discuss the generation of waves and concluded that the primary wave motion is induced by the surface-instability and the waves can subsequently become chaotic due to spatially-subharmonic and three-dimensional instabilities. In 2011, Min and Park [18] numerically investigated the wavy laminar flow with the Reynolds numbers from 200 to 1000. The wave shape predicated using their numerical model was consistent with the experimental results, which extended the application of numerical methods to the wavy film research. In addition to the wave issue, great attention has been paid on the heat and mass transfer process in falling film. An experiment was performed by Jiang *et al.* [19] to determine the effect of different liquid Reynolds numbers on falling film heat transfer. They found that the increase of liquid Reynolds number can weaken (due to increased film thickness and thermal resistance) and strengthen (due to film turbulence) the heat transfer at the same time; therefore, there should be an optimal liquid Reynolds number that balances these two contradictory effects. With the development of liquid desiccant technology, the falling film flow is attracting more attention in the air conditioning process. Feyka and Vafai [20] designed a liquid desiccant cooling system based on the falling film dehumidifier.

The system efficiency was compared to those traditional heat exchangers and its advantages were confirmed. Luo *et al.* [21] developed a new CFD predication model to study the performance of falling film based liquid desiccant dehumidifier. In their model, the dynamic heat and mass transfer process across the film interface were simulated and the impacts of various boundary conditions were investigated. In 2016, Lu *et al.* [22] proposed a CFD model to study the dynamic characteristics of solution film flow with counter-current air flow and reported that the model can be used to evaluate the dynamic development process of unsteady counter-current flow. The existing CFD tools; however, have two obvious drawbacks when dealing with the falling film problem. Firstly, the computational cost is too high and it may take even one week to calculate a typical two-dimensional case of a computation area size of $150mm \times 100mm$ [21]. Furthermore, for some special cases in which the film flow is non-continuous, the traditional CFD tools may not be appropriate due to the continuum assumption.

Since the last decades, the lattice Boltzmann method (LBM) has been gaining increasing attention and success in fundamental research and engineering applications [23, 24]. Due to its particle-based mesoscopic nature, which bridges the micro and macro worlds, LBM has shown great advantages in simulation fidelity and computational efficiency, especially for single phase and multiphase flow [25]. Generally, there are four popular LBM models so far to solve the multiphase flow problems, including the color-gradient model [26], the free energy model [27], the Shan-Chen model [28] and the phase-field model [29]. Huang *et al.* [30] compared these four models as summarized in Table 1. It can be observed that the Shan-Chen [28] and phase-field [29] models are more appropriate to solve the falling film problems

with high density ratio. Hantsch and Gross [31] numerically simulated the two-dimensional falling liquid film flow on a vertical plane using the Shan-Chen [28] two phase lattice Boltzmann model. They successfully modelled the flow with different Reynolds numbers without external disturbances. The liquid-gas density ratio in their study; however, was around 6, which was not physically meaningful [32]. Inamuro *et al.* [33] developed a high-density ratio lattice Boltzmann model based on the free energy theory, but the computational efficiency was extremely low since their model had to solve a Poisson equation during iteration. Lee and Lin [34] extended the original phase-field model by employing the stress form and potential form of the surface tension, and the improved model was able to deal with the high density issue. In their study, the liquid-gas density ratio can be increased to 1000. The model was further improved by Lee and Liu [35] by adding the isotropic discretization scheme. They applied the model to simulate a droplet colliding on dry surface and the results were reasonable. The boundary condition set in their study was periodic. Lou *et al.* [36] studied three kinds of outflow boundary conditions for two-phase LBM model, i.e. the convective boundary, the Neumann boundary and the extrapolation boundary. They found that the convective boundary condition worked well in both single phase and two-phase flow while the Neumann boundary condition and the extrapolation boundary condition produced poor results. Although great progress has been made on using LBM to simulate multiphase flow, there are still many unsolved problems especially the high density ratio and realistic boundary condition.

In this work, a new two-dimensional lattice Boltzmann model for the falling film flow under low Reynolds number (below 20) was developed. The liquid-gas density ratio can be up to 775 (i.e. the density ratio of water to air). The liquid-gas interface

with surface tension, gravity, inlet and outlet open boundary conditions as well as solid-liquid interface considering contact angles are considered in this model. The paper is organized as follows. In the section of models and methods, the lattice Boltzmann model for incompressible binary fluids, the contact angles treatment as well as boundary conditions are introduced. The results of validation tests and falling film simulation are given and discussed in the section of results and discussions, and concluding remarks are made at the end of this paper

MODELS AND METHODS

Lattice Boltzmann model for incompressible binary fluids

Cahn- Hilliard model

The model developed in this paper is based on the multi-phase lattice Boltzmann model proposed by Lee and Liu [35], and the gravity and open boundary conditions are proposed and incorporated in the original model. In this model, $\widetilde{\rho_m}$ and $\boldsymbol{u_m}$, which donate the local density and velocity of the two kinds of fluids respectively, satisfy the continuity equation

$$\frac{\partial \widetilde{\rho_m}}{\partial t} + \nabla \cdot \widetilde{\rho_m} \boldsymbol{u_m} = 0, \quad m = 1,2 \tag{1}$$

The heavier fluid is referred as Fluid 1 ($m = 1$) and the other as Fluid 2 ($m = 2$). The mixture density, $\rho = \sum_{m=1}^{2} \widetilde{\rho_m}$, should also be conserved. The composition function$C$, which is defined as $C = \widetilde{\rho_1}/\rho_1$, is then taken to describe the binary fluid, and the density can be expressed as a linear function of C

$$\rho = C\rho_1 + (1 - C)\rho_2 \tag{2}$$

According to the phase-field theory, the fluid system can be represented by a continuous variable which is known as the order parameter. In this study, the composition function C plays the role of the order parameter, and the free energy of the whole fluid system can be expressed as follows:

$$\Phi_b + \Phi_s = \int_V \left(E_0(C) + \frac{\kappa}{2}|\nabla C|^2\right) dV$$

$$+ \int_S \left(\varphi_0 - \varphi_1 C_s + \varphi_2 {C_s}^2 - \varphi_3 {C_s}^3 + \cdots\right) dS \tag{3}$$

where E_0 is the bulk energy density and usually it takes the form as $E_0 = \beta C^2(C-1)^2$, κ is a constant related with surface energy, β is a constant related with bulk energy, C_s is the composition at the solid surface. The chemical potential is defined as $\mu = \frac{\partial E_0}{\partial C} - \kappa\nabla^2 C$. The free energy is minimized when the system reaches an equilibrium state, with the result that the equilibrium interfacial profile is

$$C(z) = 0.5 + 0.5 tanh(\frac{2z}{\xi}) \tag{4}$$

where ξ is the thickness of the interface and z is the coordinate normal to the interface.

Discrete Boltzmann equations

The discrete Boltzmann equation (DBE) for the transportation of density and momentum of the mixed fluid [37, 38] is :

$$\frac{Df_\alpha}{Dt} = \left(\frac{\partial}{\partial \boldsymbol{t}} + \boldsymbol{e}_\alpha \cdot \nabla\right) f_\alpha = -\frac{1}{\lambda}\left(f_\alpha - f_\alpha^{eq}\right) + \frac{1}{{c_s}^2}(\boldsymbol{e}_\alpha - \boldsymbol{u}) \cdot \boldsymbol{F}\Gamma_a \tag{5}$$

where f_α represents the particle distribution function, $\boldsymbol{e}_\alpha$ is the velocity of particle in direction α, $\boldsymbol{u}$ is the macro velocity, c_s is the lattice sound speed and λ is the

relaxation time, $\Gamma_a = \Gamma_a(\boldsymbol{u}) = f_\alpha^{eq}/\rho$, and f_α^{eq} is the equilibrium distribution function which is defined as:

$$f_\alpha^{eq} = \omega_\alpha \rho[1 + \frac{\boldsymbol{e}_\alpha \cdot \boldsymbol{u}}{c_s^2} + \frac{(\boldsymbol{e}_\alpha \cdot \boldsymbol{u})^2}{2c_s^4} - \frac{(\boldsymbol{u} \cdot \boldsymbol{u})}{2c_s^2}] \tag{6}$$

where ω_α donating the weight factor [39].

The $\boldsymbol{F}$ in DBE is the intermolecular force and it comprises:

$$\boldsymbol{F} = \nabla \rho c_s^2 - (\nabla p - C\nabla\mu) + \rho \boldsymbol{g} \tag{7}$$

where p is the dynamic pressure which ensures the incompressibility, and $\rho \boldsymbol{g}$ is the gravity.

Two new particle distributions are defined to describe the evolution of pressure p and composition C. For pressure p we define

$$g_\alpha = f_\alpha c_s^2 + (p - \rho c_s^2)\Gamma_a(0) \tag{8}$$

and the corresponding equilibrium distribution function

$$g_\alpha^{eq} = f_\alpha^{eq} c_s^2 + (p - \rho c_s^2)\Gamma_a(0) = \omega_\alpha [p + \rho c_s^2 (\frac{\boldsymbol{e}_\alpha \cdot \boldsymbol{u}}{c_s^2} + \frac{(\boldsymbol{e}_\alpha \cdot \boldsymbol{u})^2}{2c_s^4} - \frac{(\boldsymbol{u} \cdot \boldsymbol{u})}{2c_s^2})] \tag{9}$$

The DBE for the new variable g_α is taken as

$$\frac{Dg_\alpha}{Dt} = \left(\frac{\partial}{\partial \boldsymbol{t}} + \boldsymbol{e}_\alpha \cdot \nabla\right) g_\alpha =$$

$$-\frac{1}{\lambda}\left(g_\alpha - g_\alpha^{eq}\right) + (\boldsymbol{e}_\alpha - \boldsymbol{u}) \cdot [\nabla \rho c_s^2 (\Gamma_a - \Gamma_a(0)) - C\nabla\mu\Gamma_a] \tag{10}$$

For composition C we define

$$h_\alpha = \frac{C}{\rho} f_\alpha \tag{11}$$

and the corresponding equilibrium distribution function

$$h_\alpha^{eq} = \frac{C}{\rho} f_\alpha^{eq} \tag{12}$$

The DBE for the new variable h_α is taken as

$$\frac{Dh_\alpha}{Dt} = -\frac{1}{\lambda}\left(h_\alpha - h_\alpha^{eq}\right) + M\nabla^2\mu\Gamma_a + (\boldsymbol{e}_\alpha - \boldsymbol{u}) \cdot [\nabla C - \frac{C}{\rho c_s^2}(\nabla p - C\nabla\mu)]\Gamma_a \tag{13}$$

Lattice Boltzmann equations

In this study, we choose the D2Q9 scheme so the weight factor ω_α is taken as

$$\omega_\alpha = \begin{cases} \frac{4}{9} & \alpha = 0 \\ \frac{1}{9} & \alpha = 1\sim4 \\ \frac{1}{36} & \alpha = 5\sim8 \end{cases} \tag{14}$$

and the discrete velocity $\boldsymbol{e}_\alpha$ is

$$\boldsymbol{e}_\alpha = \begin{cases} (0,0) & \alpha = 0 \\ (\pm1,0)c, (0,\pm1) & c \quad \alpha = 1\sim4 \\ (\pm1,\pm1) & \alpha = 5\sim8 \end{cases} \tag{15}$$

in which $c = \delta_x/\delta_t$ is the lattice speed, with δ_x and δ_t representing the lattice spacing and time spacing, respectively.

The discrete Boltzmann equations (10) and (13) for g_α and h_α can be integrated over time step δ_t under the D2Q9 scheme and then the lattice Boltzmann equations (LBEs) for these two distribution functions are obtained. To simplify the calculation,

two modified distribution functions $\bar{g}_\alpha, \bar{h}_\alpha$ as well as their equilibrium functions $\bar{g}_\alpha^{eq}$, $\bar{h}_\alpha^{eq}$ are introduced as follows:

$$\bar{g}_\alpha = g_\alpha + \frac{1}{2\tau}\left(g_\alpha - g_\alpha^{eq}\right) - \frac{\delta_t}{2}(\boldsymbol{e}_\alpha - \boldsymbol{u}) \cdot [\nabla^{CD}\rho c_s^2\left(\Gamma_a - \Gamma_a(0)\right) - C\nabla^{CD}\mu\Gamma_a] \tag{16}$$

$$\bar{g}_\alpha^{eq} = g_\alpha^{eq} - \frac{\delta_t}{2}(\boldsymbol{e}_\alpha - \boldsymbol{u}) \cdot [\nabla^{CD}\rho c_s^2\left(\Gamma_a - \Gamma_a(0)\right) - C\nabla^{CD}\mu\Gamma_a] \tag{17}$$

$$\bar{h}_\alpha = g_\alpha + \frac{1}{2\tau}\left(h_\alpha - h_\alpha^{eq}\right) - \frac{\delta_t}{2}(\boldsymbol{e}_\alpha - \boldsymbol{u}) \cdot [\nabla^{CD}C - \frac{C}{\rho c_s^2}(\nabla^{CD}p + C\nabla^{CD}\mu)]\Gamma_a \tag{18}$$

$$\bar{h}_\alpha^{eq} = h_\alpha^{eq} - \frac{\delta_t}{2}(\boldsymbol{e}_\alpha - \boldsymbol{u}) \cdot [\nabla^{CD}C - \frac{C}{\rho c_s^2}(\nabla^{CD}p + C\nabla^{CD}\mu)]\Gamma_a \tag{19}$$

and the LBEs for functions $\bar{g}_\alpha, \bar{h}_\alpha$ are as followed.

$$\bar{g}_\alpha(\boldsymbol{x} + \boldsymbol{e}_\alpha\delta_t, t + \delta_t) = \bar{g}_\alpha(\boldsymbol{x}, t) - \frac{1}{\tau + 0.5}\left(\bar{g}_\alpha - \bar{g}_\alpha^{eq}\right)|_{(\boldsymbol{x},t)}$$

$$+\delta_t(\boldsymbol{e}_\alpha - \boldsymbol{u}) \cdot [\nabla^{MD}\rho c_s^2\left(\Gamma_a - \Gamma_a(0)\right) - C\nabla^{MD}\mu\Gamma_a]_{(\boldsymbol{x},t)} \tag{20}$$

$$\bar{h}_\alpha(\boldsymbol{x} + \boldsymbol{e}_\alpha\delta_t, t + \delta_t) = \bar{h}_\alpha(\boldsymbol{x}, t) - \frac{1}{\tau + 0.5}\left(\bar{g}_\alpha - \bar{g}_\alpha^{eq}\right)|_{(\boldsymbol{x},t)} + \frac{\delta_t}{2}M\nabla^2\mu\Gamma_a|_{(\boldsymbol{x},t)}$$

$$+\frac{\delta_t}{2}M\nabla^2\mu\Gamma_a|_{(\boldsymbol{x}+\boldsymbol{e}_\alpha\delta_t,t)} + \frac{\delta_t}{2}(\boldsymbol{e}_\alpha - \boldsymbol{u}) \cdot [\nabla^{MD}C - \frac{C}{\rho c_s^2}(\nabla^{MD}p + C\nabla^{MD}\mu)]\Gamma_a|_{(\boldsymbol{x},t)} \tag{21}$$

The superscript “CD” and “MD” mean the central difference and the mixed difference approximation of the derivative, respectively.

After the collision process, the hydrodynamic parameters such as the composition, average velocity and dynamic pressure can be calculated by taking the zeroth and first moments of the particle distribution

$$C = \sum_\alpha \bar{h}_\alpha \tag{22}$$

$$\rho \boldsymbol{u} = \frac{1}{c_s^2} \sum_\alpha \boldsymbol{e}_\alpha \bar{g}_\alpha - \frac{\delta t}{2} C \nabla^{CD} \mu \tag{23}$$

$$p = \sum_\alpha \bar{g}_\alpha + \frac{\delta t}{2} \boldsymbol{u} \cdot \nabla^{CD} \rho c_s^2 \tag{24}$$

Treatment of contact angles

The treatment of contact angle on the solid boundary is affected by the boundary conditions for $\nabla^2 \mu$ and $\nabla^2 C$. In Lee and Liu's model [35], the boundary condition for $\nabla^2 \mu$ is taken as

$$\boldsymbol{n} \cdot \nabla \mu = 0 \tag{25}$$

where $\mathbf{n}$ is the unit vector normal to the solid boundary. The restriction on μ ensures that there is no mass flux across the solid boundary.

Lee and Liu [35] made an assumption that the fluid behavior along the solid boundary is dominated by the interactions between the solid and fluid-fluid interface, so the interactions between the solid and bulk fluids are not taken into consideration. With this assumption the cubic boundary condition for $\nabla^2 C$ as the solid boundary can be established as

$$\boldsymbol{n} \cdot \nabla C|_s = \omega (C_s - {C_s}^2) \tag{26}$$

where ω is wetting potential which reads

$$\omega = -\sqrt{2\beta/\kappa}cos\theta^{eq} \tag{27}$$

in which θ^{eq} is the contact angle.

Boundary conditions

In this falling film case, the computational domain is shown in Fig. 3. Both the solid-liquid and the liquid-gas boundaries are considered as no-slip walls, which was realized by the bounce-back scheme at the boundary nodes ($\boldsymbol{x}_s$), $f_{\bar{\alpha}}(\boldsymbol{x}_s) = f_{\alpha}(\boldsymbol{x}_s)$ ($\bar{\alpha}$ is the opposite direction of α). With this scheme the unknown variable outside the wall boundary can be approximated by

$$\phi(\boldsymbol{x}_s + \boldsymbol{e}_{\alpha}\delta t) = \phi(\boldsymbol{x}_s - \boldsymbol{e}_{\alpha}\delta t) \tag{28}$$

$$\phi(\boldsymbol{x}_s + 2\boldsymbol{e}_{\alpha}\delta t) = \phi(\boldsymbol{x}_s - 2\boldsymbol{e}_{\alpha}\delta t) \tag{29}$$

The upper (inlet) and lower (outlet) boundaries are considered as open boundaries. Velocity inlet boundary and fully developed outlet boundary were developed in this study. The validation tests were conducted to ensure the boundary conditions are appropriate. The boundary conditions are different from those adopted in Lee and Liu's [35] original work in which periodic boundary conditions were taken. Open boundary is more appropriate for the falling film simulation and so it is adopted in this work.

RESULTS AND DISCUSSIONS

First of all, three test cases were studied to validate the two-phase model. The first case was to simulate the droplets on flat plates with different contact angles to test

the approach to handling the liquid-solid interface. The second case was to simulate the typical two phase co-current flow in a channel, which has been analytically solved [30]. This case is to examine the external forces (such as gravity) added in the model. The third case aimed to test the performance of the fully developed outlet boundary by simulating a droplet flowing in an infinitely long channel. After the test cases, the dynamic process of falling film with density ratio of 775, was simulated and the results were then discussed.

Equilibrium droplet on flat plate

In this case, a rectangle computational domain with a grid size of 160×60 $(NX \times NY)$ was chosen. A two-dimensional liquid droplet with a radius of 25 was initially generated at the center of a plate. The periodic boundaries were implemented at the left and right sides and bounce back scheme was taken for the upper and lower boundary. In this case, the density ratio (the heavier over the lighter fluid, ρ^*) is taken as 100. The different contact angles $\theta^{eq} = 30°, 60°, 90°,$ $120°$ and $150°$ were simulated by choosing different wetting potential ω. The equilibrium contact angles were measured by the geometric formula of droplet height and the length of contact line. Fig. 4 shows the comparison between the measured contact angles and analytical ones. It can be observed that the angles obtained by the model agree well with the analytical ones. Furthermore, the droplet recovering process on the plate with contact angle $\theta^{eq} = 30°$ is shown in Fig. 5, in which the color represents the density while the red part and blue part are corresponding to the liquid droplet and the gas, respectively. The droplet automatically achieved equilibrium state from initial state after a short period, which indicates that the proposed model is appropriate to treat the contact angle issue.

Two-phase co-current flow in a channel

In this case, the two-phase co-current flow driven by external forces in a channel was simulated. The computational domain consisted of a 200×100 $(NX \times NY)$ rectangle girds system, while the liquid phase occupied the areas in which $NY = 0{\sim}25$ and $NY = 75{\sim}100$, and the remaining area was occupied by the gas phase. In this case, the density ratio is taken as 100, i.e. $\rho^* = 100$ The periodic boundaries were implemented at the left and right sides and no-slip walls were applied for the top and bottom boundaries, where the θ^{eq} for these two boundaries were both set as $90°$. An external force F_x was applied on the gas phase to simulate the gravity. The analytical solution for this case can be found in Huang *et al.* [30]. The velocity profiles of u_x in the channel flow obtained from the model developed in this study and the analytical solution are compared in Fig. 6. It can be observed that the velocity profiles agree well, which means the incorporation of the gravity in the proposed model is appropriate.

Droplet flowing in infinite long channel

This case aimed to test the fully developed outlet boundary condition of the proposed model. Similar to the two-phase co-current flow in a channel, a rectangle computational domain with a grid size of 200×100 $(NX \times NY)$ was chosen. A two-dimensional liquid droplet with a radius of 25 was initially generated at the left side of the domain, with an initial velocity

$$u_{x,droplet} = U, u_{y,droplet} = 0$$

$$u_{x,gas} = \ u_{y,gas} = 0$$

The channel was assumed to be infinitely long so deformation should not take place when the droplet flowed across the right boundary if the boundary was

appropriate chosen. The no-slip wall boundary conditions were applied on the upper and lower sides, and the velocity boundary was implemented on the left side. The outlet boundary, which referred the right side of the simulation domain, was set as fully developed outlet boundary. In this case, $\rho^* = 100$, Re $= \frac{2UR}{v}$. Snapshots of the droplet at different times are shown in Fig. 7. Slight deformation can be observed at the outlet while the droplet keeps the shape in the main process. Considering that falling film interface is much smoother than the droplet surface under low Reynolds number, this fully developed outlet boundary is acceptable.

Two-dimensional falling film

After the model was validated by the three cases, the model was adopted to simulate the two-dimensional falling film as shown in Fig. 3. The computational domain was also a rectangle area. As above mentioned, the upper boundary was set as velocity inlet, the lower boundary was a fully developed outlet, and both the left and right boundaries were no-slip walls. The contact angles of the left and right boundary were both set as $90°$. In this case, $\rho^* = 775$, which represents the density ratio of water and air. The initial condition was set as follows: at the very beginning, the whole simulation domain was occupied by the gas phase and then the liquid phase flows from the upper boundary with a velocity U. The velocity profile at the inlet was set as follows:

$$u_{y,liquid} = U \qquad x < h_{film}$$

$$u_{y,gas} = 0 \qquad x > h_{film}$$

$$u_{x,liquid} = \ u_{x,gas} = 0$$

The Reynolds number was defined as

$$Re = \frac{Uh_{film}}{\nu}$$

where U and h_{film} are the film velocity and film thickness at the inlet, and ν is the viscosity of the liquid. For the convenience of discussion, the dimensionless time t/t_0 is taken, where $t_0 = \rho\nu h_{film}/\sigma$ is the viscous time of the liquid phase.

A grid sensitivity test was conducted on three different grids of 30×300, 60×600, 100×1000 $(NX \times NY)$ with Reynolds number 20. Fig. 8 shows the velocity profiles of u_y at $NY = 150, t/t_0 = 1.0, Re = 20$. The velocity profile obtained on the finest grid of 60×600 agrees well with that obtained on the grid of 100×1000 except for a small fraction near the interface, which indicates that the grid of 60×600 is fine enough to capture the liquid-gas interface in this case.

Fig. 9 shows the dynamic falling film formation process with Reynolds number 20. The red part represents the liquid phase while the blue part represents the gas phase. It can be observed that the film pattern is slightly unstable and there are many small waves on the liquid interface. At the beginning, the flow is quite slow and it is then accelerated by gravity. The distance between the film heads is getting larger in the time period $t/t_0 = 1.5 - 2.0$ than $t/t_0 = 0 - 0.5$, which indicates that the average velocity of the film is increasing. The film becomes smooth and small waves disappear when it reaches the outlet at around $t/t_0 = 2.0$ and it remains unchanged after 2.5, which means the film becomes totally laminar after a short unstable period.

At $t/t_0 =$ $1.0, 1.5, 2.0$ in Fig. 9, it can be observed that separation takes place between liquid and the wall. This phenomenon is also reported in the CFD simulation done by Luo *et .al* [21] and they attributed it to the low wettability. The velocity profiles of u_y at $NY = 220$ and $NY = 260$ when $t/t_0 = 1.0, Re = 20$ are shown in Fig.

10. It can be found that separation occurs at $NY = 260$ since there are three different velocity sections while at $NY = 220$ there are only two. In both pictures we can find that the outer liquid layer always has larger velocity than the inner layer and the liquid behind ($NY = 220$) flows faster than the liquid ahead ($NY = 260$), which may result in the separation.

The film interface at the time $t/t_0 = 1.5$ for falling film with different Reynolds numbers ranging from 1 to 20 are shown in Fig. 11. It can be observed that the film patterns are quite similar, which indicates that the flow type within the Reynolds range are similar. It shows that the average velocity under different Reynolds numbers are quite close, this may be because the film is dominated by surface tension under low Reynolds number so the inlet velocity has little influence on the film flow. All of the four falling films after stabilization are totally laminar, which agree with the experimental results by Miyara [16].

CONCLUSIONS

In this paper, a new two-dimensional LBM simulation model was developed to simulate the dynamic process of falling film flow with Reynolds numbers of 1, 5, 10 and 20. The results show that the film is fully laminar under these Reynolds numbers, which agrees with the results from other researchers' work. It can be concluded that this phase-field two-phase model with gravity and open boundaries can be applied to simulate the falling film considering the high density ratio, surface tension, gravity, inlet and outlet open boundary conditions as well as contact angles. The falling film flow model developed in this study lays the foundation for the study of heat and mass transfer in the falling film based liquid desiccant dehumidifier.

ACKNOWLEDGEMENTS

The research work presented in this paper is financially supported by a grant (ECS/533212) of the Research Grant Council (RGC) of the Hong Kong SAR. The support is gratefully acknowledged.

NOMENCLATURE

C	composition of liquid phase, dimensionless
C_s	composition of liquid phase at the solid surface, dimensionless
c	lattice speed, ms^{-1}
c_s	lattice sound speed, ms^{-1}
E_0	bulk energy density, $J.m^{-3}$
$\boldsymbol{e}$	lattice discrete velocity, ms^{-1}
f	distribution function of density, $kg.m^{-3}$
$\boldsymbol{F}$	force vector, N
g	distribution function of pressure, Pa
$\boldsymbol{g}$	gravitational acceleration, ms^{-2}
h	distribution function of composition, dimensionless
h_{film}	film thickness, m
M	mobility, dimensionless
NX, NY	grid number, dimensionless
$\boldsymbol{n}$	unit vector normal to the boundary, dimensionless

p	dynamic pressure, Pa
R	radius of the droplet
Re	Reynolds number, dimensionless
S	area, m^{-2}
t	time, s
t_0	viscous time, s
U	initial velocity, ms^{-1}
$\boldsymbol{u}$	local velocity, ms^{-1}
$\boldsymbol{u}_m$	local velocity of fluid m, ms^{-1}
V	volume, m^{-3}

Greek Symbols

β	constant related with bulk energy, $J.m^{-3}$
Γ	normalized equilibrium distribution function, dimensionless
δ_x	lattice length, m
δ_t	lattice time, s^{-1}
θ	contact angle, rad
κ	constant related with surface energy, $J.m^{-3}$
λ	relaxation time, s
μ	chemical potential, $J.m^{-3}$
υ	viscosity of the liquid, ms^{-2}
ξ	interface thickness, m
ρ	density, $kg.m^{-3}$

ρ^*	density ratio, dimensionless
ρ_H	density of liquid, kg.m^{-3}
ρ_L	density of gas, kg.m^{-3}
$\widetilde{\rho_m}$	local density of fluid m, kg.m^{-3}
σ	surface tension, N.m^{-1}
τ	relaxation factor, s^{-1}
φ_0, φ_1 ...	surface energy density, J.m^{-2}
Φ_b	bulk energy, J
Φ_s	surface energy, J
ω	wetting potential, dimensionless
ω_a	weight factor, dimensionless

Subscripts

m	type of fluid in multiphase flow
s	solid surface
α	discrete direction
$\bar{\alpha}$	opposite direction of α
l	liquid phase

Superscript

CD	central difference
eq	equilibrium state
film	liquid film

gas	gas phase
liquid	liquid phase
MD	mixed difference
x, y, z	coordinates components

REFERENCES

[1] Roques, J.F. and Thome, J., Falling Films on Arrays of Horizontal Tubes with R-134a, Part I: Boiling Heat Transfer Results for Four Types of Tubes, *Heat Transfer Engineering*, vol. 28, no. 5, pp. 398-414, 2007.

[2] Roques, J.F. and Thome, J., Falling Films on Arrays of Horizontal Tubes with R-134a, Part Ii: Flow Visualization, Onset of Dryout, and Heat Transfer Predictions, *Heat Transfer Engineering*, vol. 28, no. 5, pp. 415-434, 2007.

[3] Ahn, J., Kim, J., and Kang, B.H., Performance of a Hybrid Desiccant Cooling System in a Residential Environment, *Heat Transfer Engineering*, vol. 37, no. 7-8, pp. 633-639, 2016.

[4] Lowenstein, A., Review of Liquid Desiccant Technology for Hvac Applications, *Hvac&R Research*, vol. 14, no. 6, pp. 819-839, 2008.

[5] Yin, Y., Qian, J., and Zhang, X., Recent Advancements in Liquid Desiccant Dehumidification Technology, *Renewable and Sustainable Energy Reviews*, vol. 31, pp. 38-52, 2014.

[6] Pierson, F.W. and Whitaker, S., Some Theoretical and Experimental Observations of the Wave Structure of Falling Liquid Films, *Industrial & Engineering Chemistry Fundamentals*, vol. 16, no. 4, pp. 401-408, 1977.

[7] Nakaya, C. and Takaki, R., Non-Linear Stability of Liquid Flow Down an Inclined Plane, *Journal of the Physical Society of Japan*, vol. 23, no. 3, pp. 638-645, 1967.

[8] Luo, Y., Yang, H., Lu, L., and Qi, R., A Review of the Mathematical Models for Predicting the Heat and Mass Transfer Process in the Liquid Desiccant Dehumidifier, *Renewable and Sustainable Energy Reviews*, vol. 31, pp. 587-599, 2014.

[9] Tang, R., Wang, S., Gao, D.-C., and Shan, K., A Power Limiting Control Strategy Based on Adaptive Utility Function for Fast Demand Response of Buildings in Smart Grids, *Science and Technology for the Built Environment*, vol. 22, no. 6, pp. 810-819, 2016.

[10] Jayanti, S. and Hewitt, G.F., Hydrodynamics and Heat Transfer in Wavy Annular Gas-Liquid Flow: A Computational Fluid Dynamics Study, *International Journal of Heat and Mass Transfer*, vol. 40, no. 10, pp. 2445-2460, 1997.

[11] Luo, Y., Wang, M., Yang, H., Lu, L., and Peng, J., Experimental Study of the Film Thickness in the Dehumidifier of a Liquid Desiccant Air Conditioning System, *Energy*, vol. 84, pp. 239-246, 2015.

[12] Kalliadasis, S., Demekhin, E.A., Ruyer-Quil, C., and Velarde, M.G., Thermocapillary Instability and Wave Formation on a Film Falling Down a Uniformly Heated Plane, *Journal of Fluid Mechanics*, vol. 492, pp. 303-338, 2003.

[13] Wei, M., Houser, K.W., Orland, B., Lang, D.H., Ram, N., Sliwinski, M.J., and Bose, M., Field Study of Office Worker Responses to Fluorescent Lighting of

Different Cct and Lumen Output, *Journal of Environmental Psychology*, vol. 39, pp. 62-76, 2014.
[14] Wang, L., Xiao, F., Zhang, X., and Kumar, R., An Experimental Study on the Dehumidification Performance of a Counter Flow Liquid Desiccant Dehumidifier, *International Journal of Refrigeration*, vol. 70, pp. 289-301, 2016.
[15] Shojaeefard, M.H., Zare, J., and Tahani, M., Numerical Simulation of the Thermal Performance of a Nanofluid-Filled Heat Pipe, *Heat Transfer Engineering*, vol. 37, no. 2, pp. 220-231, 2016.
[16] Miyara, A., Numerical Simulation of Wavy Liquid Film Flowing Down on a Vertical Wall and an Inclined Wall, *International Journal of Thermal Sciences*, vol. 39, no. 9-11, pp. 1015-1027, 2000.
[17] Joo, S.W. and Davis, S.H., Irregular Waves on Viscous Falling Films, *Chemical Engineering Communications*, vol. 118, no. 1, pp. 111-123, 1992.
[18] Min, J.K. and Park, I.S., Numerical Study for Laminar Wavy Motions of Liquid Film Flow on Vertical Wall, *International Journal of Heat and Mass Transfer*, vol. 54, no. 15-16, pp. 3256-3266, 2011.
[19] Jiang, B., Wang, Z., Fu, X., and Wang, Y., Experimental Study on Heat Transfer of Heated Falling Film under Gas–Liquid Cross-Flow Condition, *Heat Transfer Engineering*, vol. 35, no. 1, pp. 34-42, 2014.
[20] Feyka, S. and Vafai, K., An Investigation of a Falling Film Desiccant Dehumidification/Regeneration Cooling System, *Heat Transfer Engineering*, vol. 28, no. 2, pp. 163-172, 2007.
[21] Luo, Y., Yang, H., and Lu, L., Liquid Desiccant Dehumidifier: Development of a New Performance Predication Model Based on Cfd, *International Journal of Heat and Mass Transfer*, vol. 69, pp. 408-416, 2014.
[22] Lu, H., Lu, L., Luo, Y., and Qi, R., Investigation on the Dynamic Characteristics of the Counter-Current Flow for Liquid Desiccant Dehumidification, *Energy*, vol. 101, pp. 229-238, 2016.
[23] Perumal, D.A. and Dass, A.K., Lattice Boltzmann Simulation of Two-and Three-Dimensional Incompressible Thermal Flows, *Heat Transfer Engineering*, vol. 35, no. 14-15, pp. 1320-1333, 2014.
[24] Mishra, S.C., Poonia, H., Vernekar, R.R., and Das, A.K., Lattice Boltzmann Method Applied to Radiative Transport Analysis in a Planar Participating Medium, *Heat Transfer Engineering*, vol. 35, no. 14-15, pp. 1267-1278, 2014.
[25] Li, Q., Luo, K.H., Kang, Q.J., He, Y.L., Chen, Q., and Liu, Q., Lattice Boltzmann Methods for Multiphase Flow and Phase-Change Heat Transfer, *Progress in Energy and Combustion Science*, vol. 52, pp. 62-105, 2016.
[26] Gunstensen, A.K., Rothman, D.H., Zaleski, S., and Zanetti, G., Lattice Boltzmann Model of Immiscible Fluids, *Physical Review A*, vol. 43, no. 8, pp. 4320-4327, 1991.
[27] Swift, M.R., Osborn, W.R., and Yeomans, J.M., Lattice Boltzmann Simulation of

Nonideal Fluids, *Physical Review Letter*, vol. 75, no. 5, pp. 830-833, 1995.

[28] Shan, X.W. and Chen, H.D., Lattice Boltzmann Model for Simulating Flows with Multiple Phases and Components, *Physical Review E*, vol. 47, no. 3, pp. 1815-1819, 1993.

[29] He, X., Chen, S., and Zhang, R., A Lattice Boltzmann Scheme for Incompressible Multiphase Flow and Its Application in Simulation of Rayleigh–Taylor Instability, *Journal of Computational Physics*, vol. 152, no. 2, pp. 642-663, 1999.

[30] Huang, H.B., Huang, J.J., Lu, X.Y., and Sukop, M.C., On Simulations of High-Density Ratio Flows Using Color-Gradient Multiphase Lattice Boltzmann Models, *International Journal of Modern Physics C*, vol. 24, no. 4, pp. 1350021-1 - 1350021-19, 2013.

[31] Hantsch, A. and Gross, U., Numerical Simulation of Falling Liquid Film Flow on a Vertical Plane by Two-Phase Lattice Boltzmann Method, *Journal of Engineering*, vol. 2013, Article ID 484137, 9 pages, 2013.

[32] Hantsch, A., A Lattice Boltzmann Equation Model for Thermal Liquid Film Flow. 2013, Freiberg, Technische Universität Bergakademie Freiberg, Diss., 2013.

[33] Inamuro, T., Ogata, T., Tajima, S., and Konishi, N., A Lattice Boltzmann Method for Incompressible Two-Phase Flows with Large Density Differences, *Journal of Computational Physics*, vol. 198, no. 2, pp. 628-644, 2004.

[34] Lee, T. and Lin, C.L., A Stable Discretization of the Lattice Boltzmann Equation for Simulation of Incompressible Two-Phase Flows at High Density Ratio, *Journal of Computational Physics*, vol. 206, no. 1, pp. 16-47, 2005.

[35] Lee, T. and Liu, L., Lattice Boltzmann Simulations of Micron-Scale Drop Impact on Dry Surfaces, *Journal of Computational Physics*, vol. 229, no. 20, pp. 8045-8062, 2010.

[36] Lou, Q., Guo, Z., and Shi, B., Evaluation of Outflow Boundary Conditions for Two-Phase Lattice Boltzmann Equation, *Physical Review E*, vol. 87, no. 6, pp. 063301-1 - 063301-15, 2013.

[37] Lee, T., Effects of Incompressibility on the Elimination of Parasitic Currents in the Lattice Boltzmann Equation Method for Binary Fluids, *Computers & Mathematics with Applications*, vol. 58, no. 5, pp. 987-994, 2009.

[38] He, X.Y. and Luo, L.S., A Priori Derivation of the Lattice Boltzmann Equation, *Physical Review E*, vol. 55, no. 6, pp. R6333-R6336, 1997.

[39] He, X., Chen, S., and Doolen, G.D., A Novel Thermal Model for the Lattice Boltzmann Method in Incompressible Limit, *Journal of Computational Physics*, vol. 146, no. 1, pp. 282-300, 1998.

Table 1 Comparison of lattice Boltzmann multiphase models [30]

Model	Maximum density ratio	Efficiency	Accuracy	Pros and cons
Color-gradient	$O(10)$	Less efficient	Accurate	Only useful for density-matched cases
Shan-Chen	$O(10^2)$	Very efficient	Less accurate	Easy to implement
Free energy	$O(10)$	Less efficient	Accurate	Not convenient to specify wetting condition
Phase-field	$O(10^3)$	Efficient	Accurate	Not convenient to specify wetting condition

List of Figure Captions

Figure 1 Typical falling film

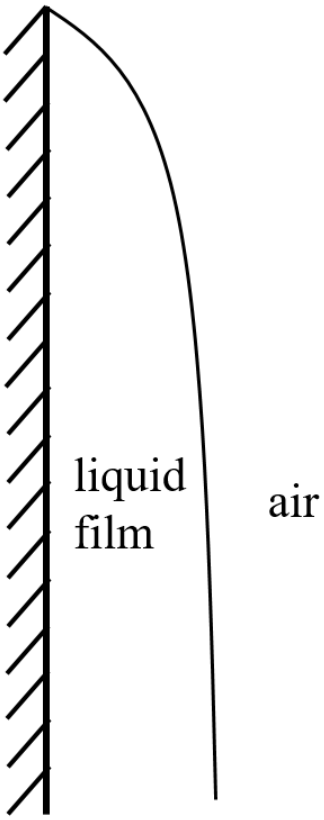

Figure 2 Schematic of the two-dimensional falling film

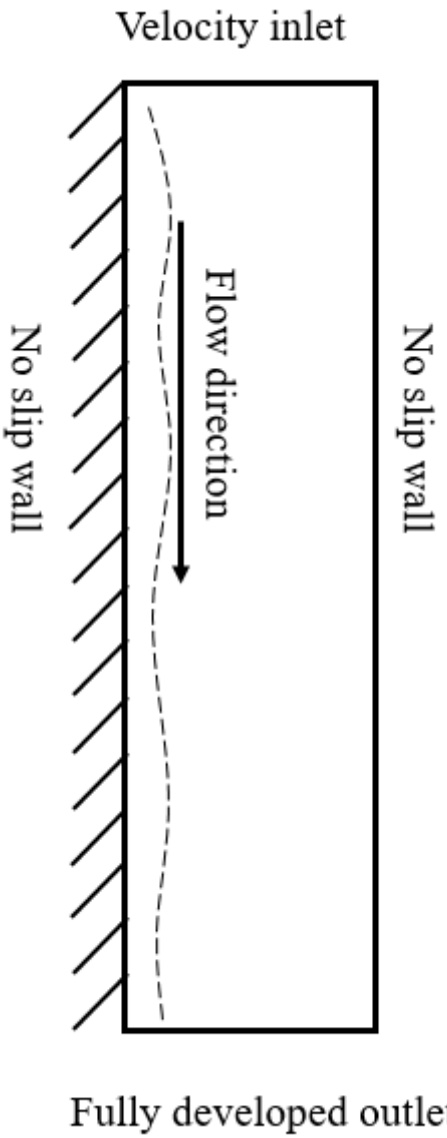

Figure 3 The computational domain of the falling film

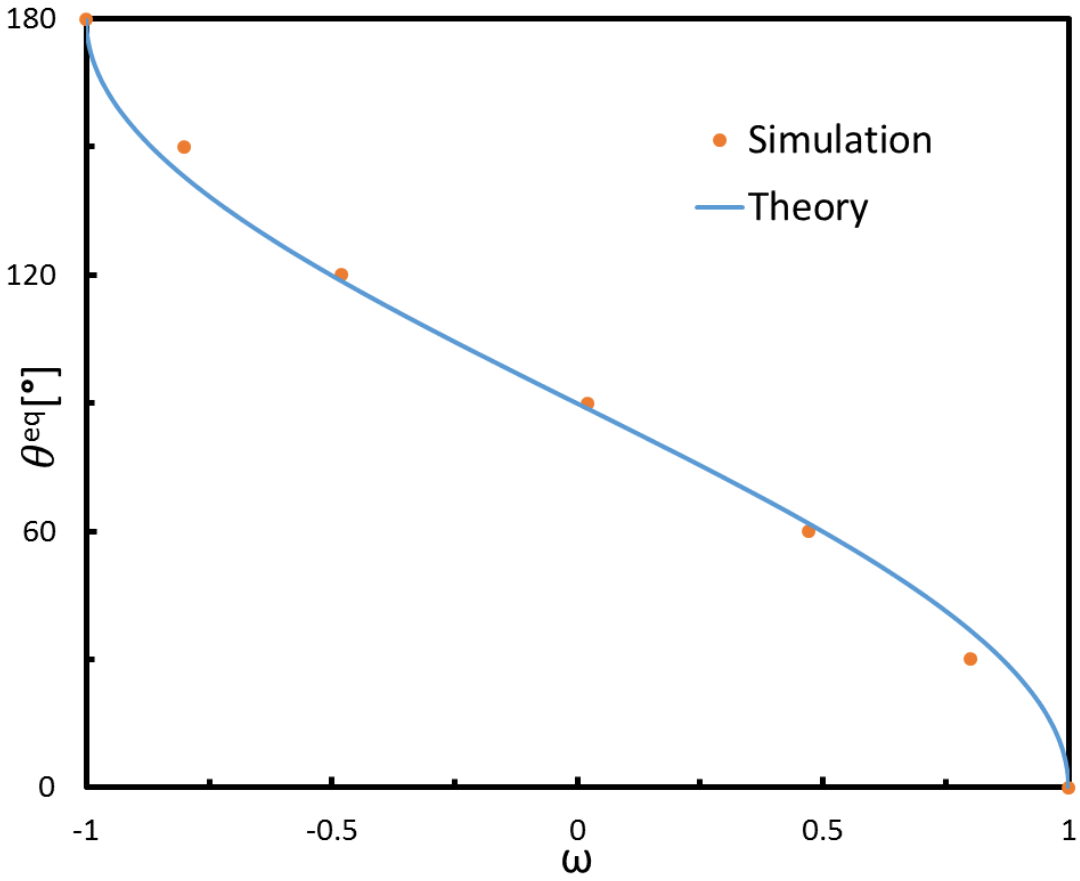

Figure 4 The comparison between the equilibrium contact angles between simulation results and analytical data

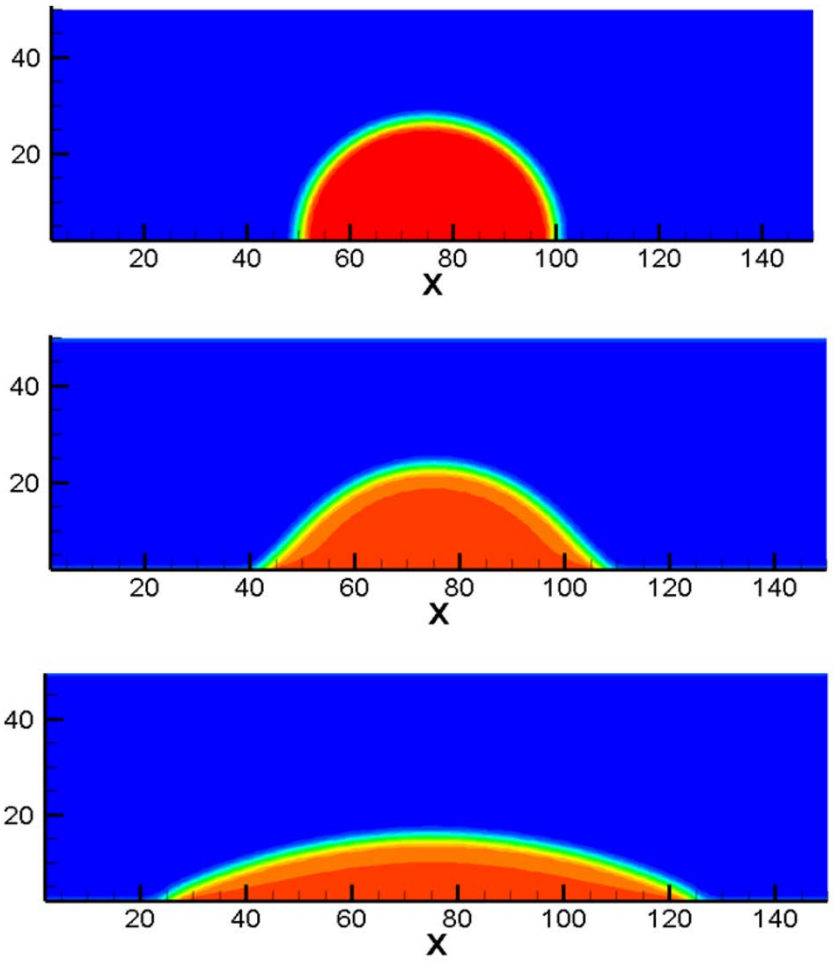

Figure 5 Droplet recovering process on the plate with contact angle 30°

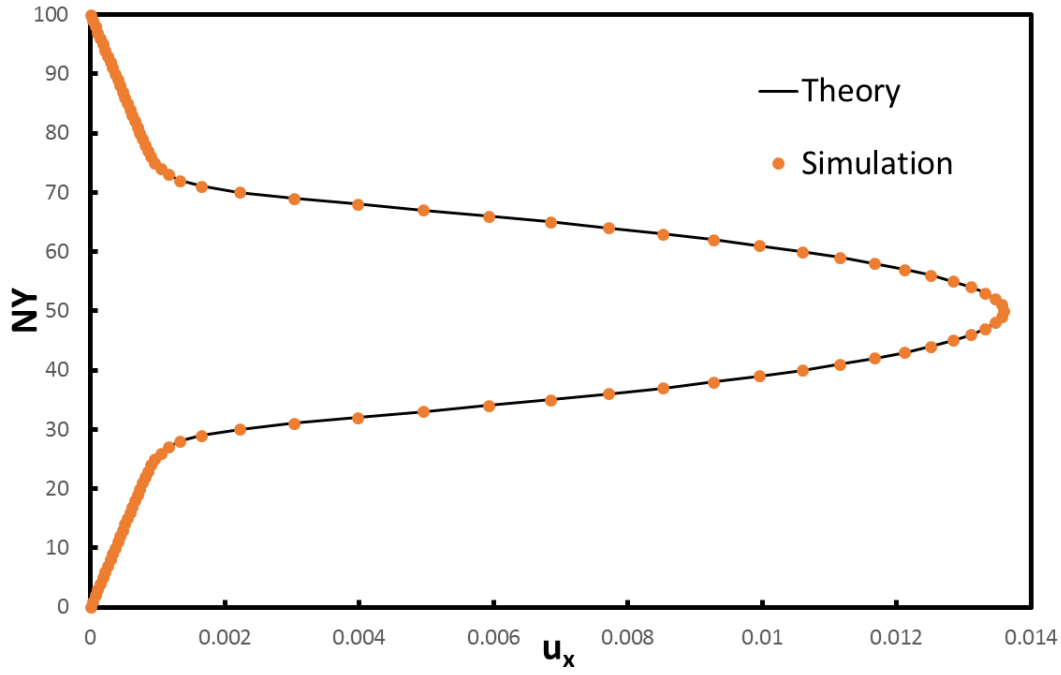

Figure 6 The comparison between the velocity profiles of u_x of co-current flow between simulation results and analytical data

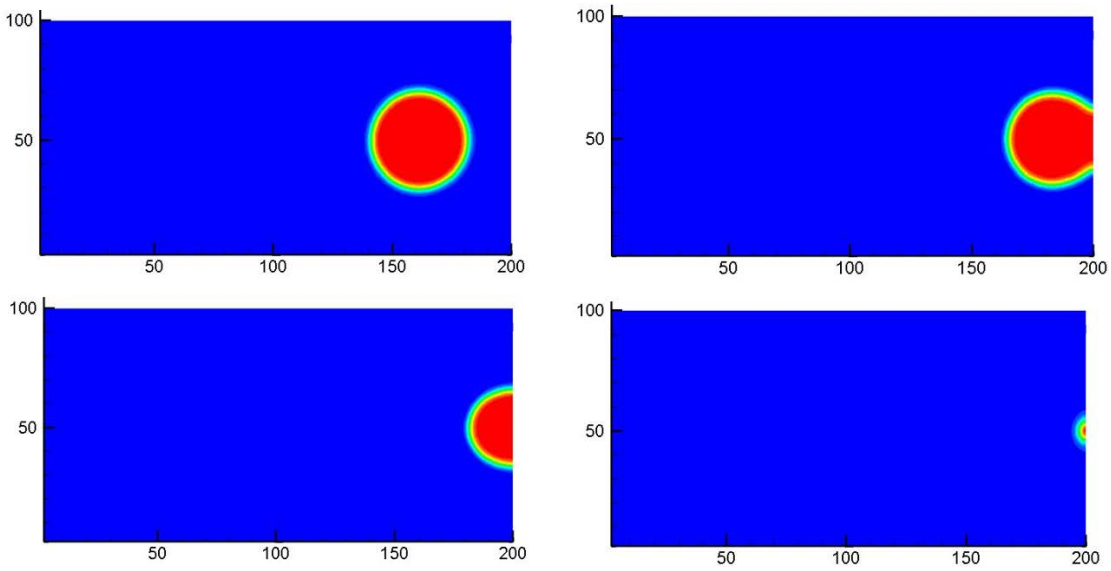

Figure 7 Snapshots of the droplet at different times

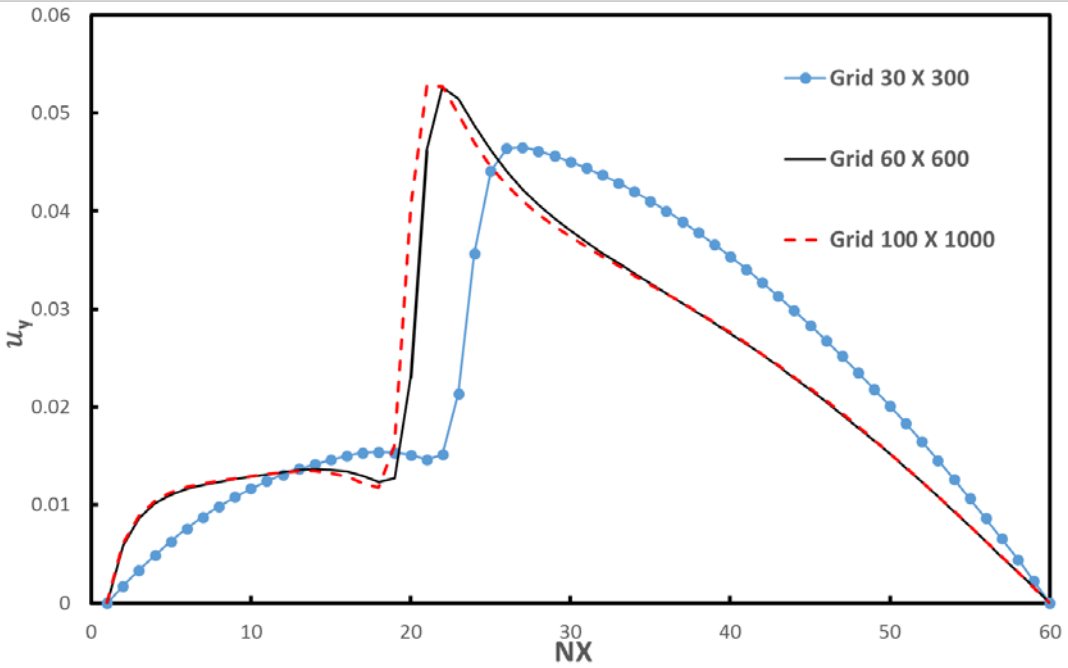

Figure 8 Grid sensitivity test for the falling film simulation at $NY = 150, Re = 20, t/t_0 = 0.5$

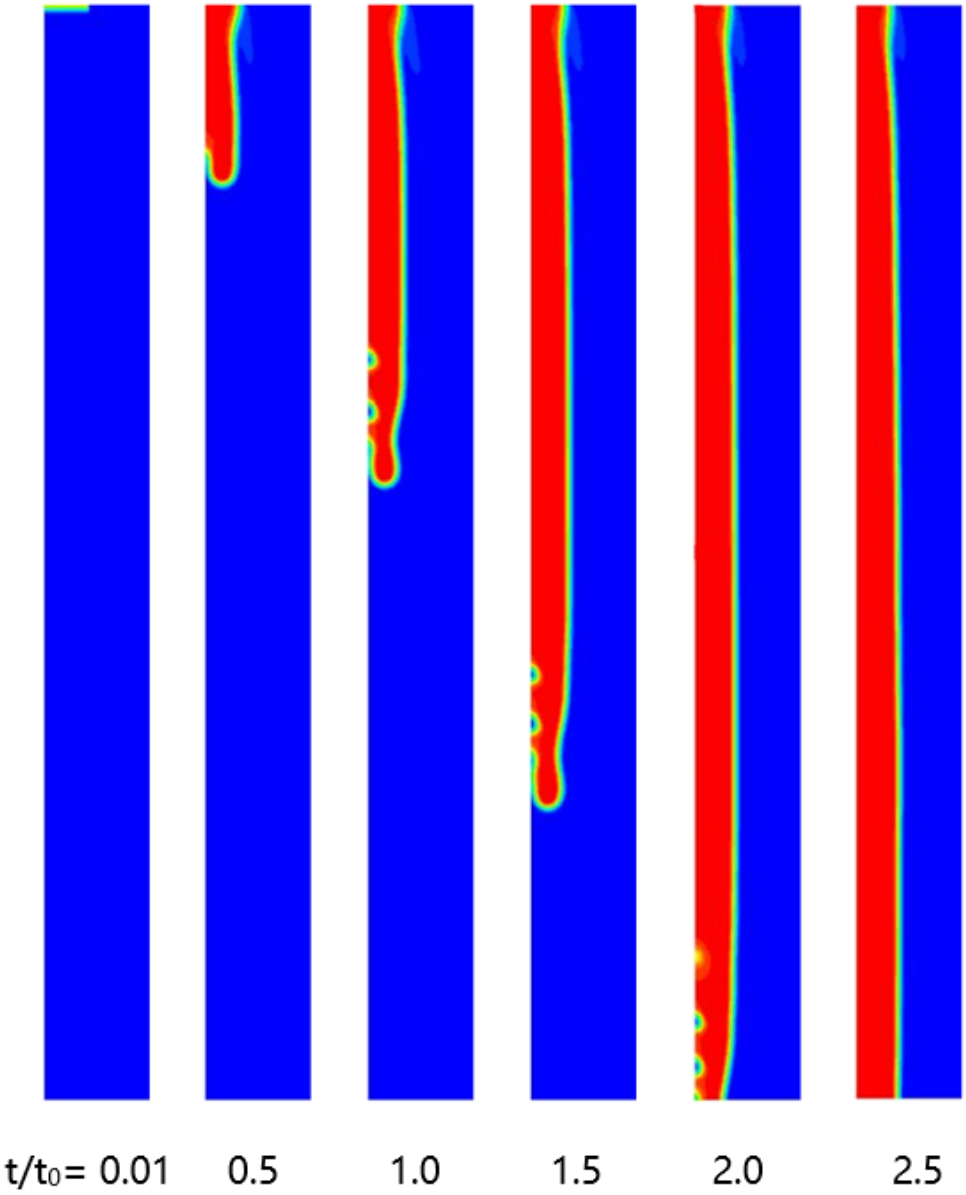

Figure 9 Time sequence of falling film with Reynolds number 20

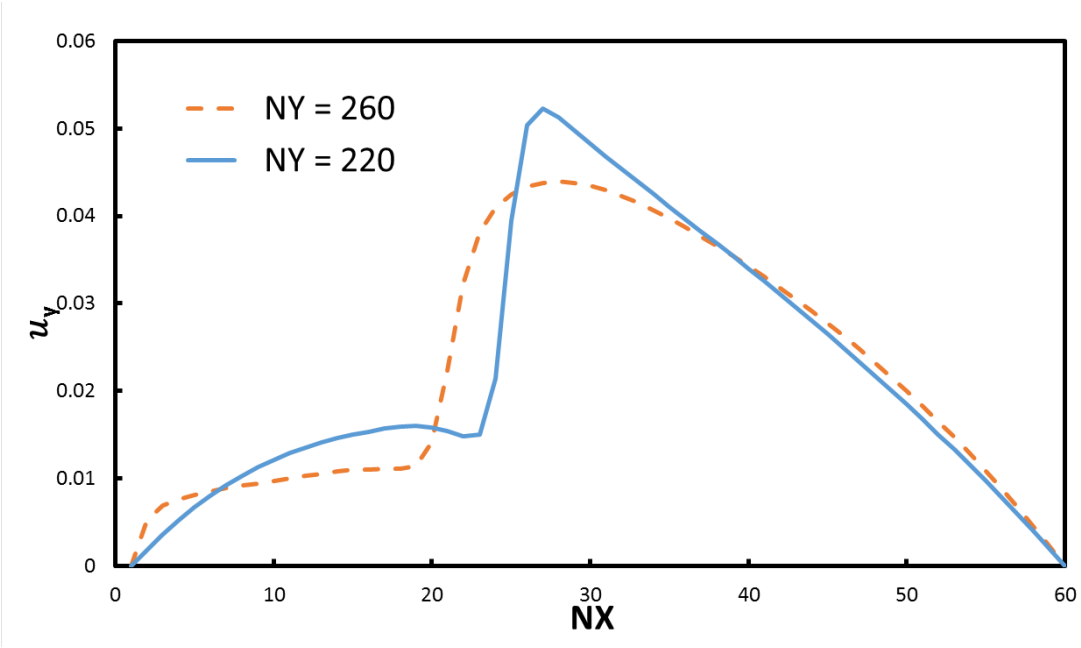

Figure 10 Velocity profiles of u_y at $NY = 220$ and $NY = 260, t/t_0 = 1.0, Re = 20$

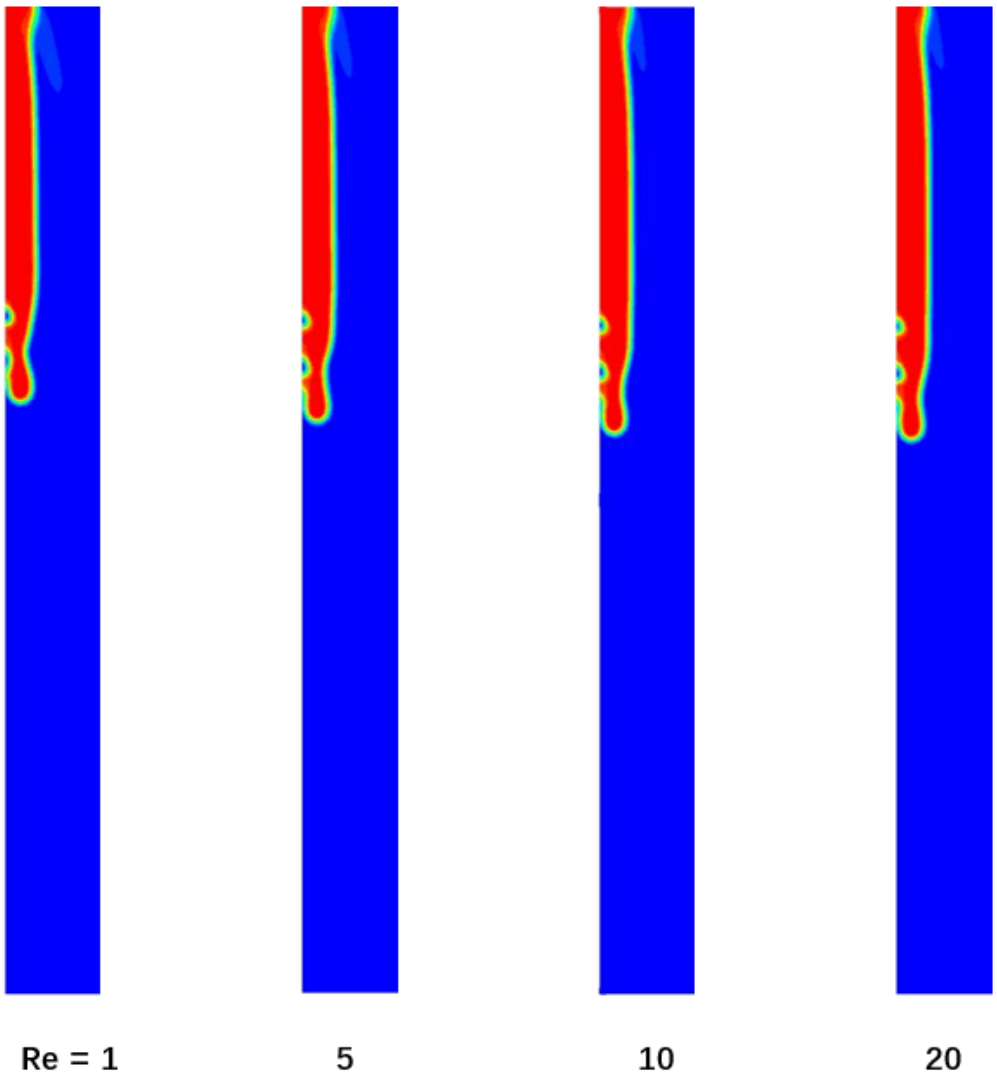

Figure 11 Film interface at $t/t_0 = 1.5$ under different Reynolds numbers